Surface Science 606 (2012) 1367–1381

Contents lists available at SciVerse ScienceDirect

Surface Science

journal homepage: www.elsevier.com/locate/susc

Structure and properties of a model oxide-supported catalyst under redox conditions: WO_x/α-Fe_2O_3 (0001)

M.E. McBriarty [a,b], M.J. Bedzyk [a,b,c], D.E. Ellis [b,c,d,*]

[a] Dept. of Materials Science & Engineering, Northwestern University, Evanston, IL 60208, United States
[b] Institute for Catalysis in Energy Processes, Northwestern University, Evanston, IL 60208, United States
[c] Dept. of Physics & Astronomy, Northwestern University, Evanston, IL 60208, United States
[d] Dept. of Chemistry, Northwestern University, Evanston, IL 60208, United States

ARTICLE INFO

Article history:
Received 25 October 2011
Accepted 23 April 2012
Available online 16 May 2012

Keywords:
Oxide surface
Metal adsorption
Density functional
X-ray standing wave
XAFS

ABSTRACT

Relaxed structures and the related electronic environments of atomic monolayers and half-monolayers of tungsten with varying degrees of oxidation on the (0001) surface of hematite (α-Fe_2O_3) are modeled using first-principles density functional theory (DFT). This report focuses on the effect of nominally oxidizing and reducing chemical environments on surface structure and chemistry. By considering the position of W atoms relative to the substrate, calculated surface structures are compared to synchrotron X-ray standing wave (XSW) imaging results recently reported for this system. The question of W valence state, previously reported as nominally W^{5+} or W^{6+} in reducing or oxidizing surroundings, respectively, is addressed and discussed in light of X-ray photoelectron spectroscopy (XPS) and extended X-ray absorption fine structure (XAFS) results to clarify the relationship between valence state, oxygen coordination, and bond lengths.

1. Introduction

Low-coverage layers of transition metals or their oxides atop oxide substrates of different compositions are of interest for various applications, most notably gas sensing and catalysis [1,2]. For oxide-supported heterogeneous catalysts, the catalytic selectivity and activity for specific reactions are defined by the composition of both the oxide substrate and the metal or metal oxide overlayer and the structure of the interface. The atomic and electronic structures of surface active sites must be well defined in order to understand the catalytic mechanism and for the rational design of reaction pathways with catalysts [3].

In previous work [4,5], density functional theory (DFT) has been combined with surface-sensitive X-ray techniques to characterize monolayer and sub-monolayer coverage vanadium oxides (VO_x) on α-Fe_2O_3 (hematite) (0001) surfaces under relevant chemical conditions. X-ray photoelectron spectroscopy (XPS) was employed to probe chemical changes when the surface was subjected to oxidizing and reducing conditions [6]. X-ray standing wave (XSW) imaging provided a sub-atomic-scale map of V positions relative to the hematite lattice under the same chemical conditions. Each of these methods revealed that chemically induced changes in the surface structure were reversible, indicating "redox reversibility", an important quality in catalytic behavior. With the use of the same experimental methodology, the structure and chemical properties of a similar heterogeneous catalyst [7], tungsten oxide (WO_x) atop the hematite (0001) surface, have recently been elucidated [8].

While XSW has provided insight on the positions of metal cations at the surface with respect to bulk cation positions, it is not possible to resolve the configuration of surface oxygen and iron atoms with the present experimental methodology. These details of surface stoichiometry and reconstruction are necessary to elucidate the chemical mechanisms underpinning catalysis and the contributions of both W and Fe, which provide acidic sites for catalytic reactions [9–11]. For example, mixed W–Fe catalysts are considered for potential heavy gas oil hydrotreatment needed for extraction of petroleum from oil sands and tars. The interactions between the two metals and with the oxide support in forming active catalytic complexes which lead to desirable activity and selectivity remain essentially unknown. In this work, DFT is employed to explore several proposed surface structures under both ideal (dry) and hydroxylated conditions. EXAFS results for 1/3 monolayer (ML) WO_x on hematite (0001) are also discussed in light of theoretical predictions based upon embedded cluster models.

Slab model DFT calculations were performed for half-ML and ML W on O- and Fe-terminated hematite (0001) surfaces. Self-consistent structural relaxations were carried out, followed by detailed density of states (DOS) calculations. After the details of the methodology are outlined, results will be presented for half-ML W coverage on O-terminated hematite (0001), revealing the consequences of varying O coordination, hydroxylation, and surface O vacancies on the surface structure and chemical properties. The effect of additional surface Fe will be discussed under the same light, as well as full ML coverage of W. After a short commentary on corrections for well-known strongly correlated electron effects in iron

* Corresponding author at: Dept. of Physics & Astronomy, Northwestern University, Evanston, IL 60208, United States. Tel.: +847-491-3665; fax: +847 491 9982.
E-mail address: don-ellis@northwestern.edu (D.E. Ellis).

0039-6028/$ – see front matter © 2012 Elsevier B.V. All rights reserved.
doi:10.1016/j.susc.2012.04.023

oxides, comparisons will be drawn between the presented calculations and recently published experimental results.

2. Methodology

The Vienna Ab Initio Simulation Package (VASP) was utilized to perform spin-polarized periodic slab DFT calculations with plane-wave basis sets [12–16]. The interactions between ionic core pseudopotentials and valence electrons were modeled using the projector augmented wave (PAW) method and corrected with the spin-polarized generalized gradient exchange-correlation approximation (GGA) as developed by Perdew and Wang (PW91) [17]. While PW91 and other gradient-corrected methods show systematic errors with respect to binding energy, bond lengths, and magnetic properties, they are in general an improvement over LSDA alone. Hybrid-functional methods which include an empirical mix of Hartree–Fock exchange and some GGA formulation at considerable additional computational cost can offer further improvements, for example in the classic case of NiO [18]. The so-called B3LYP hybrid version has been successfully applied to study the various crystallographic phases of bulk hematite [19]. However, in the absence of reliable parametrizations for complex oxide surfaces, the GGA/PW91 scheme was chosen for most computations. Grids for Brillouin zone integrations were generated automatically by the method of Monkhorst and Pack [20]. $4\times4\times1$ *k*-point meshes were found to be sufficient for all structural relaxations and densities of states (DOS) calculations, which showed no significant deviations from results using $6\times6\times1$ and $8\times8\times1$ *k*-point meshes. The computational methodology described above has been recently validated in studies of vanadium oxide on the hematite surface [4,5].

Periodic supercells were constructed by decorating the surface of a 1×1 (0001) hematite slab with W, O, and H atoms to represent surface structures under oxidizing or reducing chemical environments. The relaxed O-terminated hematite surface cell contains 19 atoms, as described in Refs. [4,5]. The bottom 4 atomic layers ($Fe–O_3–Fe_2–O_3$) were held rigid to enforce bulk boundary conditions, while all other atoms were allowed to relax via a quasi-Newtonian method or conjugate gradient algorithm [21]. The two symmetrically inequivalent low-energy surface cation sites, denoted as A and B, correspond to bulk-like cation positions. Fe atoms in these sites are denoted as Fe_A or Fe_B herein, and the same scheme is used for W (W_A, W_B). Placing W in either A or B constitutes 0.5 monolayer (ML) coverage; a full ML is considered to be both sites filled. The mixed-ML case corresponds to W occupying one site and Fe in the opposite site, e.g. Fe_A and W_B. For adsorbed O atoms, subscripts will indicate the surface site from which O is nearly vertically displaced, i.e. O_A and O_B; O_S denotes a crystal surface-layer atom. A further bulk octahedral site Fe_C is required to complete the labeling nomenclature; all sites are labeled in Fig. 1 of Ref. [4]. Thus the stacking sequence of the ideal O-terminated surface is $O_3–Fe_CFe_B–O_3–Fe_AFe_C–O_3–Fe_AFe_B…$

After structural relaxation, the electronic charge associated with each atom was determined using two different and complementary methods. Electron density was integrated over spherical volumes of variable radius R_S centered at atomic lattice positions, generating so-called Wigner–Seitz (WS) charges. This density was further projected onto the occupation of site-specific *s*, *p*, and *d* valence shells, allowing the calculation of the total density of states (DOS) of the surface cell and orbitally weighted partial densities of states (PDOS) for individual atoms. R_S values were chosen by adjusting empirical ionic radii so that the (typically overlapping) atomic volumes add approximately to the unit cell volume. In this work, R_S values were fixed at 1.6 Å for O, 0.9 Å for Fe and W, and 0.7 Å for H.

Bader topological charge analysis was also employed by way of the algorithm developed by Henkelman et al. [22]. This method describes atoms by partitioning space along zero flux surfaces of electron density, providing a complementary view of ionicity often substantially different from that of WS spherical volumes. Both WS and Bader schemes have proved to be useful in interpreting chemical bonding and the structure in molecules and solids. Both methods are used in the present work to compare the net charge on surface W atoms with nominal ionic values and calculated neighboring Fe charges under different chemical conditions. Detailed charge density maps were also prepared to display extended surface-related charge distributions and W – O covalency.

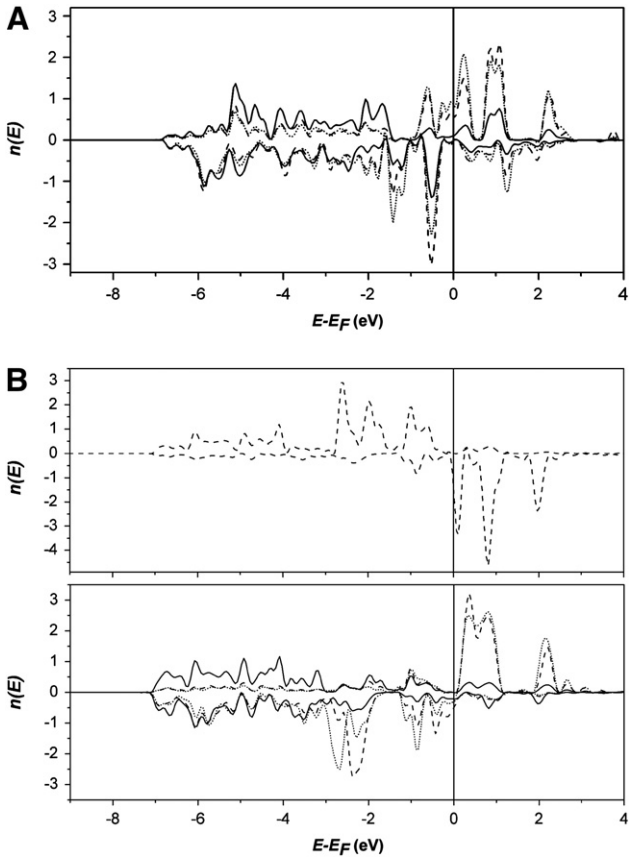

Fig. 1. (A) Surface and near-surface atoms of clean O-terminated hematite: solid line O_S, dashed Fe_C, and dotted Fe_B. Here and in following figures, $n(E)$ is the density of states for each cation or the average density of states per atom for each oxygen layer. (B) Surface and near-surface atoms of clean Fe_A-terminated hematite. Upper panel: Fe_A; lower panel: solid line O_S, dashed Fe_C, and dotted Fe_B.

In XP spectra, shifts of ~1–2 eV in core-shell energy levels are observed to indicate changes in the degree of oxidation in metals. The XP shifts of the W 4*f* core-level doublet observed by Feng et al. [8] for sub-ML WO_x/α-Fe_2O_3 (0001) are consistent with conventional interpretations of W^{5+} and W^{6+} states. W^{4+} was not observed. Excitations of core-level states create strong localized perturbations in the ground state potential which are reflected in spectral properties, including energy level shifts and wave-function distortions. Local perturbations are not easily treated in band structure methods, however, as interference between localized holes in neighboring cells influences calculated results [23]. While large supercells can in principle resolve this problem, localized molecular cluster models offer an attractive alternative. The molecular orbital description used in this approach provides an intuitive chemical interpretation of the hole-induced atomic-state changes around the excitation site. Localized-state embedded cluster methods [24] were employed herein for analyzing XPS spectra. Several cluster models, based on the ground state periodic structures, were studied.

Spectroscopic transition energies, which are rigorously differences in *total energy* between initial and final states, can be quantitatively approximated in the Slater transition state (TS) scheme as the differences between *one-electron energies*, defined by the TS Hamiltonian [25]. In its simplest form the TS Hamiltonian is derived by an expansion of the total energy in a Taylor series of the orbital occupation numbers as $H^* = (H_i + H_f)/2$, i.e., the average of initial and final state Hamiltonians.

This procedure is easily implemented in Hartree–Fock and DFT codes, and it is used in the present work to model shifts in W *4f* XP spectra.

3. Results

The interlayer spacings of clean hematite surfaces with different oxygen coverages calculated by the model used herein are in good agreement with previously calculated data by Bergermayer et al. [26] and Jin et al. [4], as shown in Table 1. This comparison and previous studies using the same methodology on vanadium oxide-terminated hematite surfaces [4,5] lend confidence to the computational procedures used in this work.

A cross-section of relaxed structures with varying coverages of W and Fe with/without coadsorbed oxygen is given in Figures below. The partial densities of states (PDOS) given in Fig. 1A and B show the very different energy landscapes of the clean oxygen- vs. iron-terminated hematite (0001) surfaces. These are the ground-state surfaces expressed under different oxidizing conditions as proposed by Wang et al. [27]. Understandably, in the former case, the O *sp* valence band (VB) of width ~7 eV dominates, showing strong ionic-covalent mixtures from subsurface Fe_B and Fe_C sites which induce a small net magnetism. This phenomenon is in agreement with theoretical results for the (0001) hematite surface obtained from different methodologies in Ref. [27]. In the latter case, strong magnetic features of the Fe_A terminal layer are evident in occupied states within 3 eV of the Fermi energy E_F and in the low-lying excited state region.

3.1. Half-monolayer W

3.1.1. O-terminated substrate: 0, 1/3 and 1 ML coadsorbed oxygen

Structures with varying degrees of oxygen coadsorption were investigated for 0.5 ML W adsorbed to a clean O-terminated hematite surface (terminal layers O_3–Fe–… are referred to as (I) in the following). Here, a single W atom was placed in either the A or B cation surface site (W_A, W_B) of a 1×1 supercell, and the opposite surface site was kept empty. These surfaces were then modeled with 0, 1/3, and 1 ML of overlayer-adsorbed O′ to study the adsorption and oxidation states of surface-bound tungsten. In addition to the c-axis dislocations discussed throughout, and in experimental emphasis, nontrivial x- and y-dislocations are also predicted, which may amount to more than 1 Å in highly nonsymmetric and defected sites. Nevertheless, it remains generally possible to clearly identify A- and B-site cation origins. Structural data derived from selected ground-state periodic cells, including interlayer and interatomic distances, are provided in Tables 2 and 3. The predicted cohesive energy and W net charge, as determined from both R_S volume integration and Bader schemes, are provided in Table 4 for these structures and additional unstable isostoichiometric structures with lower predicted cohesive energy. Included for comparison are results from our predictions for W in bulk WO_3.

If bulk-like hematite stacking was to continue up from the O-terminated surface, the next Fe^{3+} ion would occupy the Fe_A site, residing over the hollow in the cation layer below it. One might expect, therefore, that W_A would be energetically favored over W_B. However, the energetic preference for surface W position depends on oxygen coverage: with either no adsorbed O′ or a complete monolayer O'_3, B-site W_B is preferred by about 0.4 eV. However, for the case of a single adsorbed O′, corresponding to 4-fold W – O coordination, the A-site is preferred by over 0.8 eV.

With no coadsorbed O′, the PDOS for W_A and W_B, Fig. 3A and B respectively, show some similarity in the form of extensive broad features extending to ~8 eV below E_F representative of covalent mixing with the oxygen VB as verified in the charge analysis below. W_A shows strong spin-polarization doublets just below and above E_F while such features are mostly absent from the W_B spectrum. Examination of Fig. 3A shows a coherent spin superposition of W_A, Fe_B, Fe_C, and O_S, where the W response is dominated by superexchange coupling through its three ligands to neighboring Fe moments. In oxides this coupling normally results in antiferromagnetic coupling to the dominant Fe moments, but here this is apparently not the case. The unexpected behavior in the W_A surface is perhaps due to the unusually low coordination and rather large distance to neighboring Fe, in contrast to W_B (Fig. 3B), which sits below the surface O′, with short W – $Fe_{B/C}$ distances. In principle W polarization can be sensed by spectroscopic means; moreover, the net W moment is negligible, as expected. The surface O_S and subsurface Fe_B and Fe_C PDOS are recognizable as those of hematite (Fig. 1A) but are significantly distorted by the adsorbed cation. Coadsorption of O, as in O'_AW_A (Fig. 3C), causes a compression of the W PDOS, effectively opening a gap ~3 eV around E_F due to its strong overlap/interaction with the rather localized O′ band starting ~2 eV below E_F. This W_A gap is spectral evidence of oxidation relative to the initial metal-terminated state in vacuum.

Due to increasing charge transfer from W to O, the volume-integrated cation charges would be expected to increase with rising W – O coordination number; however, no significant change is found in the W charge within a fixed-radius WS sphere, denoted as Q_{WS}(W). This might be attributed to over-counting of electrons, since the radius of integration R_S is fixed at 0.9 Å, compared to the empirical W^{6+} radius of 0.74 Å and the unknown but presumably larger radius for W^{5+}. Another traditional measure of transition metal valence state is the *d*-electron population: here, it is expected to change from 1 to 0 electron for the transition from W^{5+} to W^{6+}. The R_S volume integration (Table 4A) indicates a larger and less variable *d* occupancy (1.23 *e* in WO_3 vs. 1.48 *e* for the low coordination W_A site), essentially due to the formation of strong covalent interactions with the ligands, as mentioned in the context of partial densities of states. Bader charge analysis shows somewhat greater variation with environment. Bader charges on W, denoted as Q_B(W),

Table 1
Comparison of surface and near-surface layer relaxations in the z direction (%, relative to bulk) for ideal (clean) hematite (0001) surface configurations and with 1/3 ML coadsorbed oxygen. Subscripts indicate the cation lattice position (A, B, C) or anion occupation number of the plane (3) as well as the layer: t (terminal), S (surface), or S-1 (sub-surface). I denotes oxygen terminated surface; O′ denotes coadsorbed oxygen.

Surface identifiers:	I: O_3 – Fe			II: Fe_A-I			III: O'_AFe_A-I	
	I[a]	I[b]	I[c]	II[a]	II[b]	II[c]	III[a]	III[c]
Layers								
$O_{3t}[/O_{1t}]$ – Fe_{At}							+87.4	+88.6
O_{3t} – Fe_{Bt}	−4.9	−5.8	−6.7					
Fe_{Bt} – Fe_{At}	−78.4	−73.0	−72.7					
Fe_{At} – O_{3S}	+34.7	+30.6	+32.7	−51.3	−59.4	−53.6	−18.8	−18.3
O_{3S} – Fe_{CS}	−7.1	+4.5		+6.4	+5.8	+7.6	+4.6	+6.0
Fe_{CS} – Fe_{BS}	+17.4			−31.7	−46.0	−38.4	−50.7	−58.9
Fe_{BS} – O_{3S-1}	−3.5			+13.1	+9.7	+14.7	+18.8	+18.8

[a] After Ref. [26].
[b] After Ref. [4].
[c] Present work.

Table 2
Calculated interlayer distances R_L (Å) for various W and O adsorption scenarios on hematite (0001). Surface identifiers indicate adsorbate sites with underlying (I) surface termination; O′ represents overlayer oxygen. For Fe, subscripts t, B, and C refer to terminal sites and surface/near-surface B and C sites, respectively. Subscript notation is as described in Table 1. Numbers in parentheses indicate the standard deviation of the z-positions (last digit) in the oxygen plane of interest. If no such number is present, the standard deviation is less than 0.005 Å.

Surface identifiers for columns in Table:

1: W_A	2: W_B	3: O'_AW_A	4: O'_3W_B	5: $O'_BFe_BW_A^{(a)}$
6: $O'_AW_AFe_B$	7: $O'_AFe_AW_B$	8: $O'_BW_BFe_A$	9: $O'_{AB}W_BFe_A$	10: $O'_3W_BFe_A$
11: W_AW_B	12: $O'_{AB}W_AW_B$	13: $O'_3W_AW_B$	14: W_AO_V	15: W_AO_{V2}
16: W_BO_{V3}	17: $W_AFe_BO_V$	18: $W_AFe_BO_{V2}$	19: $W_AFe_BO_{V3}$	20: HO'_AW_A
21: $(HO')_3W_B$	22: $HO'_BW_BFe_A$	23: $(HO')_{AB}W_AFe_B$	24: $(HO')_3W_AFe_B$	

(a) In this case, one surface O is displaced to the O′ position (see text).

(A) Adsorbed cations on oxygen terminated substrate I = O_3 – Fe…. Coadsorbed oxygen is designated as O′, with subscripts indicating site/occupancy.

Surface	1	2	3	4	5	6	7	8	9	10
O′ – W	–	–	1.73	0.7 (4)	1.49	1.69	1.63	1.68	1.12 (1)	0.71
O′ – Fe_t	–	–	–	–	1.18	2.16	0.81	2.56	1.30 (1)	1.26
W – Fe_t	–	–	–	–	−0.31	0.47	−0.82	0.88	0.18	0.55
W – O_S	0.43	−0.4(3)	0.66	1.95 (8)	0.34 (6)	0.8 (4)	0.2 (6)	0.8 (5)	1.2 (5)	1.55
Fe_t – O_S	–	–	–	–	0.65 (6)	0.3 (4)	1.0 (6)	−0.0 (5)	1.0 (5)	1.00
O_S – Fe_C	1.26	1.3(3)	1.16	0.82 (8)	1.30 (6)	1.3(4)	1.6 (6)	1.3 (5)	1.2 (5)	0.86
Fe_C – Fe_B	0.34	1.46	0.33	0.28	0.49	0.82	0.68	0.81	0.64	0.66
Fe_B – O_{S-1}	0.90	0.2(2)	0.93	0.99	0.80 (5)	0.60 (5)	0.65 (3)	0.58 (7)	0.73 (3)	0.81

(B) Monolayer W_AW_B overlayer with and without coadsorbed oxygen.

Surface	11	12	13
O_t – W_A	–	1.7 (5)	1.10 (9)
O_t – W_B	–	1.1 (5)	0.94 (9)
W_A – O_S	1.21	1.0 (3)	1.22 (4)
W_B – O_S	0.29	1.6 (3)	1.37 (4)
O_S – Fe_C	1.39	1.1 (3)	1.08 (4)
Fe_C – Fe_B	0.90	0.62	0.56
Fe_B – O_{S-1}	0.47	0.74 (3)	0.79 (4)

(C) W and bimetallic W and Fe adsorption on defected/reduced (oxygen vacancy O_V) (I) surfaces. O_{V3} represents a fully depleted O_3 surface layer, i.e., metallic Fe termination.

Surface	14	15	16	17	18	19
Fe_t – W	–	–	–	0.97	0.96	1.45
O_S – W	0.9 (1)	0.93	–	1.0 (1)	1.19	–
O_S – Fe_t	–	–	–	0.0 (1)	0.23	–
O_S – Fe_C	0.9 (1)	1.00	–	1.0 (1)	1.41	–
W – Fe_C	0.05	0.06	1.13	0.04	0.22	−0.01
Fe_t – Fe_C	–	–	–	1.01	1.18	1.44
Fe_C – Fe_B	0.27	−0.07	0.90	1.39	1.08	0.39
Fe_B – O_{S-1}	1.1 (1)	1.2 (1)	0.49	0.3 (3)	0.3 (5)	0.87 (5)

(D) Protonated mono- and bi-metallic surface resulting in hydroxyl-bonded tungsten.

Surface	20	21	22	23	24
H – O′	0.56	−0.3 (7)	−0.12	0.4 (2)	0.6 (5)
O′ – W	1.91	1.0 (2)	1.58	1.9 (2)	1.4 (2)
O′ – Fe_t	–	–	2.22	1.9 (2)	1.0 (2)
W – Fe_t	–	–	0.65	−0.03	−0.34
W – O_S	0.66 (4)	1.3 (2)	0.6 (8)	0.9 (5)	1.00 (9)
Fe_t – O_S	–	–	−0.1 (8)	0.9 (5)	1.33 (9)
O_S – Fe_C	1.27 (4)	1.0 (2)	1.7 (8)	1.6 (5)	1.13 (9)
Fe_{CS} – Fe_B	0.42	0.66	0.48	0.60	0.51
Fe_B – O_{S-1}	0.80 (1)	0.78 (5)	0.80 (5)	0.65 (7)	0.79 (3)

range from 3.02 *e* for WO_3 to 2.06 *e* for the W_A surface site. The W_B site and O′W coadsorbed states show intermediate $Q_B(W)$ values; in accordance with qualitative expectations, increased oxygen coordination leads to increased W net charge. We note that, in the various environments considered here, $Q_B(W)$ (see Table 4) appears to be approximately one-half of the nominal oxidation state. However, the predicted oxidation state remains ambiguous for the 1/3 ML and 1 ML O′ structures; it is unclear whether the related cation formal charge would be +6, as in bulk WO_3, or a partially reduced +5 surface state, as inferred from core-level XPS (discussed below). The value of $Q_B(W)$ does not change greatly as the W – O coordination number increases from 4 to 6 in these cases, calling into question the simple assumption that increased O coordination always yields a more oxidized cation.

Bond lengths of the surface structures are presented in Table 3, in order to explore connections between structure, charge, and apparent oxidation state. Only the energetically favored structures for each stoichiometry are presented in this Table; a considerable number of additional structures were also analyzed. The W – O bond lengths are very

Table 3
Interatomic distances R_{ij} (Å) for half-monolayer W deposited on O_3- and Fe-terminated hematite (0001) surfaces. Atom labels and surface identifiers are same as defined in Table 2. Upper and lower limits are given for varying bond lengths. Surface identifiers 1, 2, 3… are the same as in preceding tables. Interaction lengths greater than 3.25 Å are not reported.

(A) Surface identifiers are as given in Table 2.

Surface	1	2	3	4	5	6	7	8	9	10
O′ – W	–	–	1.73	1.75–1.79	1.81	1.73	1.89	1.73	1.8	1.79
O′ – Fe_t	–	–	–	–	1.93	>3.25	1.88	>3.25	1.95–1.99	2.00–2.01
W – Fe_t	–	–	–	–	2.54–2.79	2.46, 3.10	2.56	2.48	2.55–2.79	2.94
W – O_S	1.80	1.78–1.80	1.84	2.09–2.58	1.89	1.88–1.94	1.80–1.96	1.86–1.97	1.87–2.35	2.18–2.19
Fe_t – O_S	–	–	–	–	1.94–2.01	1.80–1.99	1.91–2.14	1.80–1.91	1.88–1.92	1.99–2.00
O_S – Fe_C	2.08	1.93–2.07	2.04	1.76–1.86	2.09	2.03–2.17	2.04–2.08	2.03–2.26	1.93–2.33	1.95–1.96
O_S – Fe_B	2.27	>3.25	2.19	1.81–1.90	2.11	2.27	2.02	2.15	2.05–2.16	2.16–2.17
W – $Fe_{(B/C)}$	>3.25	2.36, 2.75, 3.10	>3.25	3.10	2.57, 3.10	>3.25	2.59–2.94	2.9–3.10	3.10	3.08
Fe_t – $Fe_{(B/C)}$	–	–	–	–	2.65	2.48	>3.25	2.70	>3.25	>3.25

(B) Surface identifiers are as given in Table 2.

Surface	11	12	13
O_t – W_A		1.87	1.83–2.05
O_t – W_B		1.72–1.99	1.80–2.00
W_A – W_B	3.03	2.73–2.92, 3.22	2.55, 3.08–3.09
W_A – O_S	1.98	1.87–2.13	2.00–2.19
W_B – O_S	1.91	2.02–2.69	2.02–2.23
O_S – Fe_C	2.1	2.06–2.10	2.05–2.13
O_S – Fe_B	>3.25	2.11, 2.29	2.20, 2.26
W – $Fe_{(B/C)}$	2.58	>3.25	3.04

(C) Surface identifiers are as given in Table 2. The subscripts (B/C)S and (A/C)S-1 refer respectively to surface and sub-surface sites.

Surface	14	15	16	17	18	19
W – Fe_t	–	–	–	2.63	2.55, 2.88	2.74
W – $O_{S,S-1}$	1.85–2.17	1.93–2.13	>3.25	1.92–2.16	1.89–2.01	2.03–2.09
Fe_t – $O_{S,S-1}$	–	–	–	1.91, 2.03	1.92	>3.25
O_S – Fe_{CS}	1.99, 2.13	2.03	–	2.01, 2.11	2.22	–
O_S – Fe_{BS}	1.99	2.02	–	>3.25	>3.25	–
W – $Fe_{(B/C)S,\ (A/C)S-1}$	2.54–2.78, 3.05–3.12	2.53, 2.54, 2.97–3.02	2.03, 3.10	2.56–2.65, 3.00–3.07	2.64–2.80, 3.07	2.66–2.99, 3.12
Fe_t – $Fe_{(B/C)S,\ (A/C)S-1}$	–	–	–	2.42, 2.63	2.32	2.19, 2.44

(D) Surface identifiers are as given in Table 2.

Surface	20	21	22	23	24
H – O′	0.97	0.98–1.02	1.00	0.99, 1.00	0.97–0.99
O′ – W	1.92	1.77–2.11	1.89	1.80	2.08–2.13
O′ – Fe_t	–	–	>3.25	1.99	2.05–2.13
W – Fe_t	–	–	2.32	2.62, 2.70	2.56, 3.04
W – O_S	1.79–1.80	1.88–2.21	1.83–2.09	1.82–2.02	1.86–1.97
Fe_t – O_S	–	–	1.82–1.94	1.92–2.02	2.04–2.36
O_S – Fe_C	2.1	1.85–1.96	1.96, 2.00	1.95, 2.12	2.02–2.08
O_S – Fe_B	2.30, 2.38	1.97, 2.25	2.06	2.10	2.23, 2.31
W – $Fe_{(B/C)}$	>3.25	2.98	2.75	>3.25	>3.25
Fe_t – $Fe_{(B/C)}$	–	–	2.68	>3.25	>3.25

similar between the 3-fold O_S-coordinated W_B-(I) and 4-fold O′W_A-(I) cases. The terminal O′ in the 4-fold case has the shortest W – O bond length, indicating a stronger covalency, while the bond lengths between W and the surface O_3 layer increase by only 0.04–0.06 Å versus the 3-fold case. There is an insignificant difference in Bader charges (2.79 vs. 2.77 *e*) between 4-fold O′W_B and the nominally saturated O′$_3W_B$ 6-fold case with a complete O′ overlayer; similar values (2.73 vs. 2.75 *e*) are observed for W_A. This seemingly anomalous oxidation behavior, indicating nearly identical chemical state of W in these four cases, may be explained by the W – O bond length variations. For the relaxed O′$_3W_B$-(I) case the underlying WO_3 tetrahedron (Fig. 2H) is heavily distorted, with only one W – O_S bond shorter than the longest W – O distance calculated for bulk WO_3 (2.13 Å). The W – O′ distances, however, are comparable to the bond lengths observed for the 3- and 4-fold cases. W might then be considered to be 4-fold coordinated in this highly distorted case. Table 2A shows the distances between relaxed atomic layers at and near the surface. For the relaxed 3-fold W_B-(I) case, as seen in Fig. 2E,F, W sits *below* the surface O layer, screened from the vacuum. However, this puts strain on the underlying B-site cation, and so the distance between sub-surface Fe atoms is remarkably higher than that of the more oxidized cases.

A volume-rendered ground state electron density map for the surface region of the simplest W_A-(I) configuration is shown from two perspectives (a birds-eye view of multiple cells from within the interslab region toward the surface) in Fig. 4. The density levels displayed were chosen to highlight the covalent character of metal–oxygen interactions as seen both in W_A – O_S bond regions and in Fe – O lobes (side cuts in Fig. 4a). The adsorbed W is easily identified by its three-fold coordination to substrate oxygens. With the exception of the W – O lobes, a notable feature, found by examining a variety of density maps for varying compositions and geometries, is the lack of clear differentiation between valence density around the W- as opposed to Fe-sites.

The predicted relative homogeneity of cation densities shows the considerable ability of valence electrons to screen the differently charged cations (here, nominally W^{5+}, but note that Bader charge suggests a value closer to 4+ vs. Fe^{3+}) and provides a reminder that available (unoccupied) states are perhaps most important for describing reactivity with incoming molecules and atoms. Such vacant states are not visible in conventional (i.e. ground-state) density maps such as Fig. 4. Nevertheless, ground-state density maps are of considerable value in the presence of symmetry-breaking atomic and molecular adsorbates, which will be considered elsewhere.

Table 4
Comparison of electronic charge Q (in elementary charge units, *e*) and supercell binding energy E_B (eV/cell) of W and Fe cations in the A and B surface sites for oxygen-terminated substrate O_3–Fe (I) with various adsorbed oxygen coordinations, compared to bulk-like Fe in an undecorated hematite slab and W in bulk WO_3. Note that in the case $O'Fe_BW_A$ one underlying O is displaced to the surface; see Table 2 and text. Q_{WS} indicates the R_S integrated cation charge and related *s*, *p*, and *d* orbital populations; Q_B indicates the Bader-analysis ionic charge. The nominal configuration for WO_3 is W^{+6} $s^0p^6d^0$.

(A) WO_3 bulk, W adsorption and O′W coadsorption on (I); alternate cation site vacant.

Surface	WO_3	W_A	W_B	$O_A'W_A$	O'_BW_B	O'_3W_A	O'_3W_B
E_B	–	152.18	152.62	161.95	161.11	171.11	171.29
Q_{WS}(W)	5.50	5.34	5.38	5.41	5.41	5.40	5.40
s	0.03	0.04	0.04	0.04	0.04	0.04	0.04
p	5.21	5.14	5.16	5.18	5.18	5.16	5.16
d	1.23	1.48	1.42	1.38	1.38	1.40	1.40
Q_B(W)	3.02	2.06	2.30	2.73	2.79	2.75	2.77

(B) Fe_2O_3 bulk and bimetallic Fe and W adsorption on (I) with no and 1/3 ML coadsorbed oxygen. Subscript br denotes bridging oxygen.

Surface	Fe_2O_3	W_AFe_B	W_BFe_A	$O'_BW_AFe_B$	$O'_AW_AFe_B$	$O'_{br}W_AFe_B$	$O'_AW_BFe_A$	$O'_BW_BFe_A$	$O'_{br}W_BFe_A$
E_B	–	159.83	159.02	167.65	168.00	167.38	167.94	167.98	167.85
Q_{WS}(W)	–	5.37	5.32	5.41	5.38	5.40	5.39	5.39	5.39
s		0.04	0.04	0.04	0.03	0.03	0.03,	0.03,	0.03
p		5.15	5.14	5.17	5.17	5.17	5.17	5.17	5.17
d		1.44	1.50	1.38	1.42	1.41	1.40	1.41	1.41
Q_B(W)	–	1.81	2.02	2.50	2.41	2.31	2.34	2.40	2.34
Q_{WS}(Fe)	3.13	2.93	2.83	2.88	2.80	2.95	2.94	2.93	2.87
s	0.06	0.07	0.07	0.08	0.08	0.06	0.06,	0.08	0.06
p	5.85	5.83	5.83	5.82	5.85	5.82	5.83	5.85	5.83
d	4.96	5.17	5.27	5.22	5.27	5.17	5.17	5.15	5.24
Q_B(Fe)	1.64	0.83	1.07	0.83	0.81	1.03	1.26	0.98	1.14

(C) Bimetallic Fe and W adsorption on (I) with 2/3 and 1 ML coadsorbed oxygen.

System	$O'_{AB}W_AFe_B$	$O'_{AB}W_BFe_A$	$O'_3W_AFe_B$	$O'_3W_BFe_A$
E_B	176.03	176.08	183.59	183.94
Q_{WS}(W)	5.41	5.41	5.47	5.45
s	0.04	0.04	0.04	0.04
p	5.18	5.18	5.20	5.19
d	1.38	1.37	1.30	1.33
Q_B(W)	2.61	2.64	2.88	2.86
Q_{WS}(Fe)	3.03	3.04	3.12	3.13
s	0.07	0.07	0.07	0.06
p	5.86	5.85	5.86	5.86
d	5.05	5.05	4.95	4.95
Q_B(Fe)	1.31	1.32	1.67	1.69

(D) Monolayer W_A, W_B adsorption on (I) with 0, 2/3 and 1 ML coadsorbed oxygen.

System	W_AW_B	$O'_{AB}W_AW_B$	$O'_3W_AW_B$
E_B	161.04	180.41	190.09
$Q_{WS}(W_A)$	5.29	5.40	5.42
s	0.03	0.03	0.03
p	5.11	5.16	5.18
d	1.57	1.41	1.36
$Q_B(W_A)$	1.23	2.08	2.51
$Q_{WS}(W_B)$	5.35	5.37	5.42
s	0.03	0.03	0.03
p	5.14	5.15	5.19
d	1.48	1.46	1.37
$Q_B(W_B)$	1.44	1.93	2.53

(E) W_A and W_B adsorption on defected/reduced (oxygen vacancy) (I) surfaces, ranging over single vacancy O_V, divacancy O_{V2}, and fully depleted O_{V3} oxygen layer.

System	W_AO_V	W_BO_V	W_AO_{V2}	W_BO_{V2}	W_AO_{V3}	W_BO_{V3}
E_B	145.31	143.69	136.34	134.78	124.04	124.95
Q_{WS}(W)	5.42	5.33	5.40	5.31	5.37	5.27
s	0.03	0.04	0.03	0.04	0.03	0.04
p	5.17	5.12	5.16	5.08	5.14	5.05
d	1.38	1.51	1.41	1.57	1.47	1.64
Q_B(W)	2.16	1.63	1.79	0.86	1.17	0.17

(F) Bimetallic Fe and W adsorption on defected/reduced (oxygen vacancy) (I) surfaces.

System	$W_AFe_BO_V$	$W_BFe_AO_V$	$W_AFe_BO_{V2}$	$W_BFe_AO_{V2}$	$W_AFe_BO_{V3}$	$W_BFe_AO_{V3}$
E_B	152.21	151.24	143.77	142.90	134.57	132.87
Q_{WS}(W)	5.40	5.33	5.36	5.34	5.37	5.27
s	0.03	0.04	0.03	0.04	0.03	0.04
p	5.16	5.12	5.14	5.11	5.14	5.07
d	1.41	1.52	1.46	1.52	1.46	1.62
Q_B(W)	1.77	1.30	1.41	0.90	1.14	−0.03

Table 4 (*continued*)

(F) Bimetallic Fe and W adsorption on defected/reduced (oxygen vacancy) (I) surfaces.

System	$W_AFe_BO_V$	$W_BFe_AO_V$	$W_AFe_BO_{V2}$	$W_BFe_AO_{V2}$	$W_AFe_BO_{V3}$	$W_BFe_AO_{V3}$
Q_{WS}(Fe)	3.00	2.99	2.92	2.94	2.95	3.02
s	0.07	0.07	0.09	0.07	0.09,	0.07
p	5.83	5.82	5.82	5.83	5.80,	5.80
d	5.11	5.13	5.17	5.16	5.15	5.10
Q_B(Fe)	0.79	0.77	0.30	0.46	0.00	0.34

(G) Single hydroxyl co-adsorption with mono- and bi-metallic adsorbed (I) surfaces.

System	HO'_AW_A	HO'_BW_B	$HO'_AW_AFe_B$	$HO'_BW_AFe_B$	$HO'_BW_BFe_A$	$HO'_AW_BFe_A$
E_B	165.01	164.83	171.21	170.76	171.41	171.26
Q_{WS}(W)	5.38	5.41	5.38	5.39	5.40	5.38
s	0.04	0.04	0.03	0.04	0.03	0.04
p	5.17	5.18	5.16	5.15	5.16	5.15
d	1.42	1.38	1.42	1.42	1.40	1.43
Q_B(W)	2.77	2.71	2.31	1.94	2.15	1.98
Q_{WS}(Fe)	–	–	2.86	3.09	2.89	3.06
s			0.08	0.06	0.08	0.07
p			5.85	5.84	5.85	5.84
d			5.22	5.01	5.19	5.04
Q_B(Fe)	–	–	0.72	1.32	0.85	1.38

(H) Multiple hydroxyl co-adsorption with mono- and bi-metallic adsorbed (I) surfaces.

System	$(HO')_{AB}W_AFe_B$	$(HO')_{AB}W_BFe_A$	$(HO')_3W_A$	$(HO')_3W_B$	$(HO')_3W_AFe_B$	$(HO')_3W_BFe_A$
E_B	183.10	183.01	186.83	186.93	194.88	194.54
Q_{WS}(W)	5.39	5.39	5.55	5.49	5.44	5.43
s	0.03	0.03	0.03	0.04	0.03	0.03
p	5.17	5.17	5.22	5.20	5.19	5.19
d	1.40	1.41	1.19	1.27	1.34	1.35
Q_B(W)	2.34	2.67	2.96	2.93	2.60	2.59
Q_{WS}(Fe)	2.91	2.88	–	–	2.97	2.90
s	0.06	0.06			0.05,	0.06
p	5.84	5.84			5.83	5.83
d	5.18	5.22			5.15	5.21
Q_B(Fe)	1.06	1.05	–	–	1.32	1.31

3.1.2. Hydroxyl termination

For many catalytic reactions, hydrogen will be present in some form (e.g. H_2, H_2O, NH_3, or hydrocarbons) in the reactor. Furthermore, in the experimental redox studies on the present system, hydrogen was used as the reducing agent. It is therefore important to investigate the effects of adsorbed hydrogen on the surface structure and chemistry. Hydrogen atoms were placed above the terminal oxygen atoms to simulate hydroxyl groups, and the structures were relaxed. Structural results for 1/3 ML hydroxylated O-terminated surfaces are given in Tables 2D and 3D. There is a 180 meV preference for HO'_AW_A (pictured in Fig. 5A,D) vs. HO'_BW_B, as reported in Table 4G. While this site ordering agrees qualitatively with that found for the O'_AW_A vs. O'_BW_B case (840 meV), the energy preference is significantly weaker.

The key structural difference noted is in the W_A-O' bond length, which extends by 0.19 Å for the hydroxyl ligand, while the W_A-O_S bonds contract by about 0.05 Å. These bond length dilations and

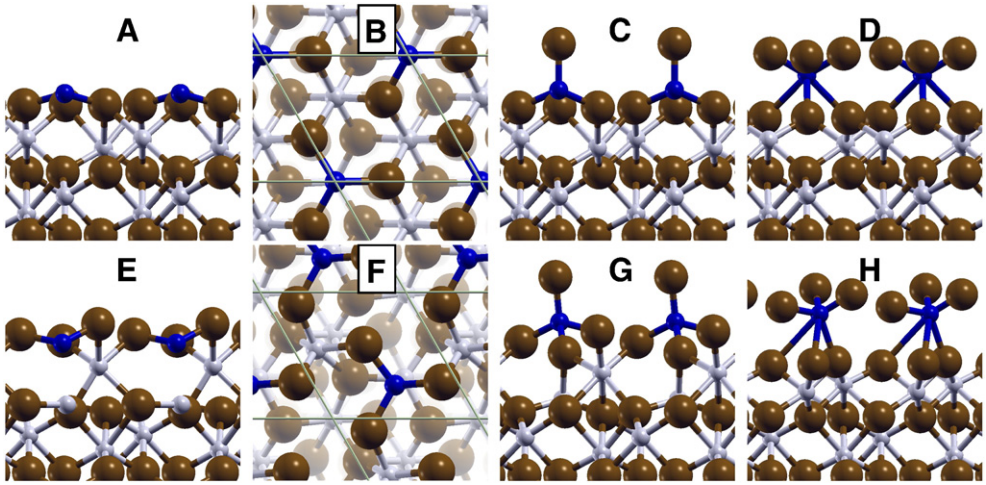

Fig. 2. Three-, four-, and six-fold coordinated 1/2 ML W O-terminated structures representing 0, 1/3 and 1 ML coadsorbed oxygen. Top row shows (A) side view of W_A, (B) top view of W_A, (C) side view of 1/3 ML O′ on W_A, and (D) side view of 1 ML O′ on W_A. Bottom row shows (E) side view of W_B, (F) top view of W_B, (G) side view of 1/3 ML O′ on W_B, and (H) side view of 1 ML O′ on W_B. W atoms are shown in blue; Fe, gray; and O, brown, with lines showing the supercell boundaries in (B) and (F). Graphics for this and the following structure figures were prepared with the XCrySDen program (http://www.xcrysden.org). Atomic coordinates used in calculations may be found in Online Supplemental Material.

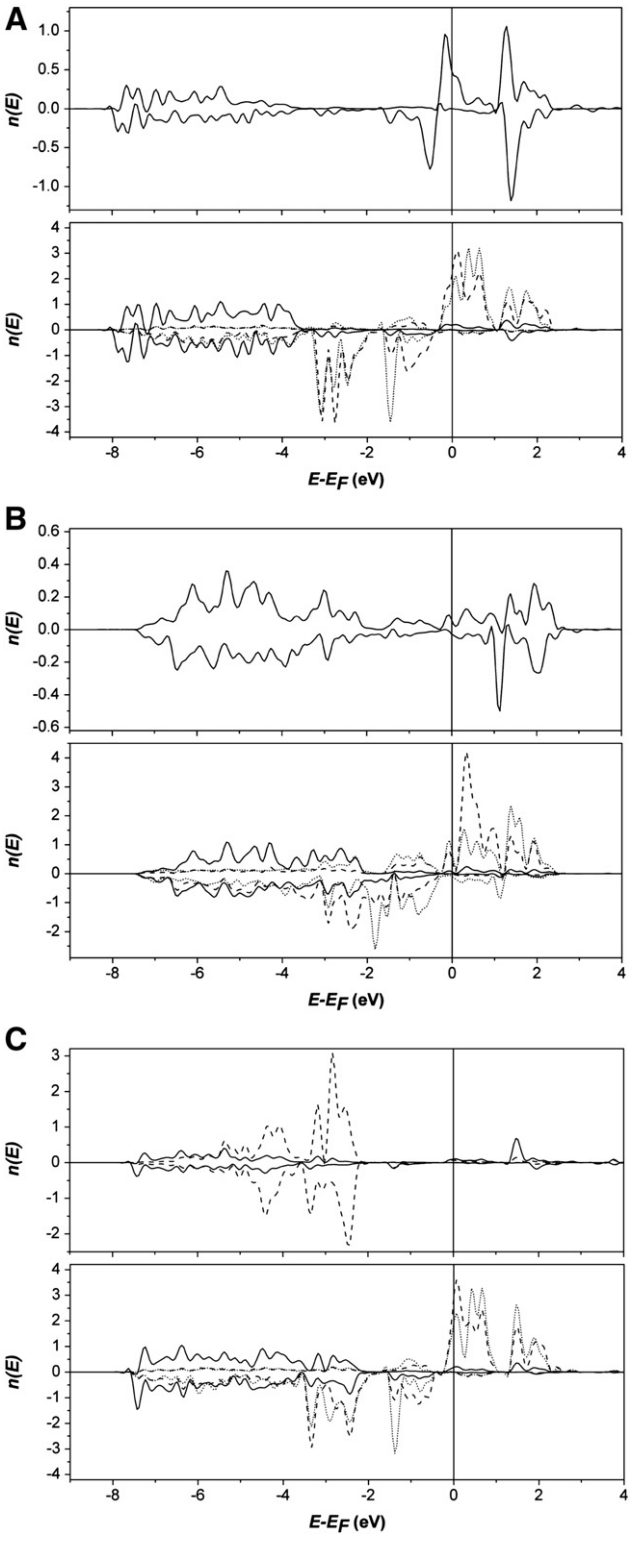

Fig. 3. (A) 1/2 ML W_A on O-terminated hematite. Upper panel, W_A; lower panel, solid O_S, dashed Fe_C, and dotted Fe_B. (B) 1/2 ML W_B on O-terminated hematite. Upper panel, W_B; lower panel, solid O_S, dashed Fe_C, and dotted Fe_B. (C) Surface and near-surface atoms of O'_AW_A (1/2 ML W_A, 1/3 ML O′) on O-terminated hematite. Upper panel, solid W_A and dashed O'_A; lower panel, solid O_S, dashed Fe_C, and dotted Fe_B.

contractions appear to chemically compensate for each other, since the W_A Bader charge is hardly affected (2.73 vs. 2.77 *e*). PDOS for the model HO'_AW_A are given in Fig. 6, with features similar to those of O'_AW_A already discussed. The O′ VB is somewhat broadened and shifted to lower energy by interaction with H, shifting the W covalent components downward in turn. While the top of the W VB ends at ~4 eV below E_F, a small amount of W conduction band character now appears near E_F.

After the surface has been in contact with a humid environment, higher hydroxyl coverages may be expected. Results for saturated $(HO')_3W$ surfaces are shown in Tables 2D, 3D, and 4H. As in the case of O'_3W, there is little effect of the cation surface site on its chemical state. Bader charges, although (counterintuitively, see below) ~0.2 *e* more positive than the O terminations, vary little: 2.96 (W_A) vs. 2.93 *e* (W_B). Volume charges Q_{WS} also show the six-fold coordinated $(HO')_3W$ cations to be more positive, by ~0.1 *e*, compared to the four-fold hydroxylated complexes, mostly due to a reduced W 4*d* covalency in the hydroxylated complexes. These electronic structure changes accompany significant shifts in position relative to the underlying lattice and in W–O bond lengths; for example, R(W–O′) changes from 1.91 Å (4-fold $HO'W_A$) to 1.77–2.11 Å (6-fold $(HO')_3W_B$), and R(W–O_S) lengthens, on average, from 1.79–1.80 Å to 1.77–2.11 Å. With saturated 1 ML HO′ ligation, W_B is favored over W_A (by 100 meV), although less strongly than in the O'_3W case (180 meV). The W_B cation coordination for 1 ML OH ligation is closer to that of bulk WO_3 than its O'_3W_B surface counterpart, as expected due to the saturation of O bond valence.

3.2. Effects of surface O vacancies (reducing environment)

Surface cations in metal oxides have been shown to be highly catalytically active in the presence of surface O defects [28,29]. Thus, the consequences of a "reduced" O-defective surface were studied for different cation configurations. Structures were calculated with 1/3, 2/3 or all O_3 atoms removed from the surface anion layer, denoted as O_V, O_{V2}, and O_{V3}. Due to the 3-fold symmetry of the O plane in hematite, there was generally a small energetic and structural difference between the three different possible O-defective configurations; the lowest-energy structures (usually varying by only ~1 meV) for each different surface cation arrangement and stoichiometry are reported herein. Structural details of energetically preferred cases with depleted surface O layers of each stoichiometry are presented in Tables 2C and 3C. Converged energies and calculated surface cation charges are shown in Table 4E.

Starting with the 1/2 ML W coverage, we find that the W_B site which is most favored on the O_3-terminated substrate is replaced by O_VW_A as the lowest energy 1/3 ML vacancy controlled surface with a large advantage of 1.62 eV over O_VW_B. Structurally, this suggests that during a reduction reaction, W_B sitting 0.37 Å below the O_3 layer is displaced to the A-site and sits ~0.9 Å above the oxygen plane. The bond lengths W–O_S, initially 1.79–1.80 Å, increase to 1.85–2.17 Å. Other near-surface bonds involving Fe–O and W–Fe are affected, but less strongly; e.g., W–Fe, initially 2.32–3.06 Å, increases to 2.54–3.12 Å. These metal–metal distances are sufficiently short to permit significant bonding interaction. Concerning charge distribution, the W Bader charge decreases as 2.23 > 2.16 > 1.63 *e* for W_B, W_AO_V, and W_BO_V respectively with decreasing coordination and increasing bond lengths. As an extreme example of distortion, the more highly reduced $W_BFe_AO_{V2}$ configuration shows a W dislocation of ~1.8 Å away from registry; such sites, if non-periodic, may be 'invisible' to the XSW diffractive probe. As W–O_S coordination decreases, the corresponding reduction of W is apparent in the lengthening of bond lengths R(W–O_S): 1.79–1.80 (W_B(I)) < 1.85–1.91 (W_AO_V) < 1.93 Å (W_AO_{V2}). Systematic reductions in W Bader charges are also observed, with the [Q(W_A), Q(W_B)] charges being [2.16, 1.63] > [1.79, 0.86] > [1.17, 0.17] *e* for (I), O_V, and O_{V2} cases, respectively. For the W_BO_{V3} case, W_B has no near oxygen coordination; this is in contrast to W_A, which is coordinated with at least one O atom, even in the mixed metal terminated $W_AFe_BO_{V3}$ case (see Sec. 3.4). This is reflected in the anomalously large z-spacing between W_B and the underlying Fe_C atom, which in all other cases is <0.22 Å but here is greater than 1.1 Å.

In summary, for the less-reduced O_S-terminated cases, W_A is preferred by about 1.6 eV; however, when the substrate O_3 layer is completely removed, the preference shifts to W_B. W_A is also generally more oxidized; indeed, the Bader charge (0.17 *e*) on the fully O-depleted W_BO_{V3} case

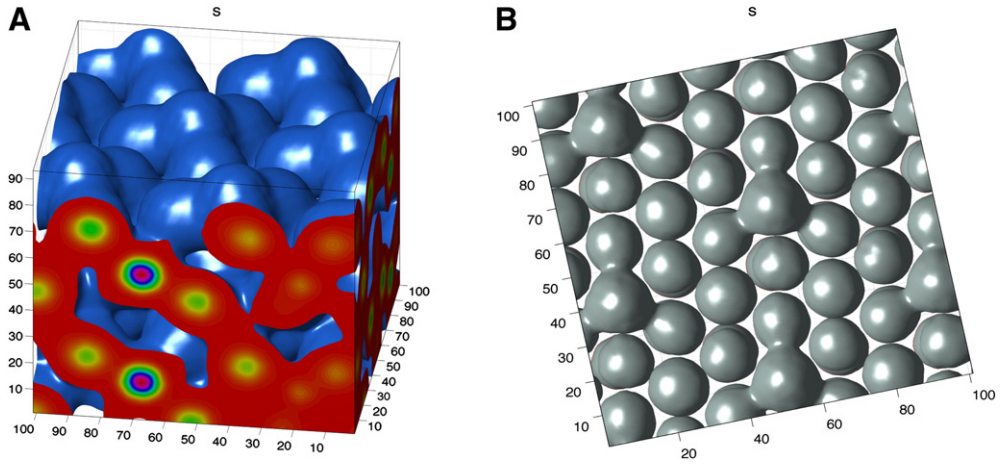

Fig. 4. (A) Side view and (B) top view of a volume-rendered valence electron density map of 1/2 ML W_A adsorbed on O-terminated hematite (0001) surface. Surface W_A can by identified by its three-fold covalent bonding lobes to O_S.

indicates that W is metallic, compared to W_AO_{V3} (1.17 *e*). In the W_BO_{V3} case, W_B sits well above the Fe layer instead of being part of a mixed metal surface layer, as in every other case. The surface O_S atoms are clearly a controlling factor in transverse positioning of W, as the more oxygen deficient surfaces show greater displacements away from bulk cation registry.

3.3. Full-monolayer metal coverage

3.3.1. Mixed W and Fe coverage

The complex interaction between different metal atoms in redox reactions can be exploited to generate high yields and selectivity towards specific products in bimetallic catalysts. The Fe-terminated hematite surface is therefore particularly interesting for bimetallic catalytic surface studies. Both W_AFe_B and W_B Fe_A configurations were investigated, corresponding to 1/2 ML of each cation on a so-called mixed-ML surface. Surface annealing leading to cation migration under reaction conditions could allow for reconstructions with both configurations; recall that Fe_A and W_B are separately favored under 1/2 ML conditions. O′ overlayer coverages of 0, 1/3, 2/3, and 1 ML were modeled in order to explore different levels of metal oxidation. Geometric details of selected stable mixed-ML surfaces are provided in Tables 2A and 3A. Three comparable 1/3 ML O′ structures are presented here, but only the most stable isostoichiometric structures are given for the 0, 2/3, and 1 ML O′ cases.

For the metal-terminated cases with no coadsorbed oxygen, the addition of surface Fe_B appears to stabilize W_A in the W_AFe_B-(I) case. However, this stabilization is at the expense of the surface O_3 layer symmetry: one O atom moves above both the surface Fe and W species, leaving a vacancy O_V in the surface layer (Fig. 7A). In contrast, the 1 ML O'_3 case shows relatively high symmetry, with nearly flat O planes and consistent interatomic distances (Fig. 7C).

Coverage-dependent behavior is also observed for the preferred surface cation positions. In bulk hematite, an Fe_A cation sits 0.63 Å below an Fe_B. However, the surface cation order in this mixed-ML case depends on the O′ adsorption site in the 1/3 ML O′ overlayer cases. In these examples, if the starting configuration before relaxation has O′ placed above the A- or B-site cation, then that cation rises to a higher z-position after relaxation. For the stable cases with higher O′ coverage, however, the regular cation configuration is restored, with Fe_AW_B preferred. For the 2/3 ML O′ cases, both W and Fe are vertically coordinated with one O′ atom before relaxation. In the W_AFe_B case, the O′ atoms relax to highly regular tetrahedral coordination to the cations, which also rise to practically the same height (Fig. 7C). However, in the W_BFe_A case, the O′ atoms

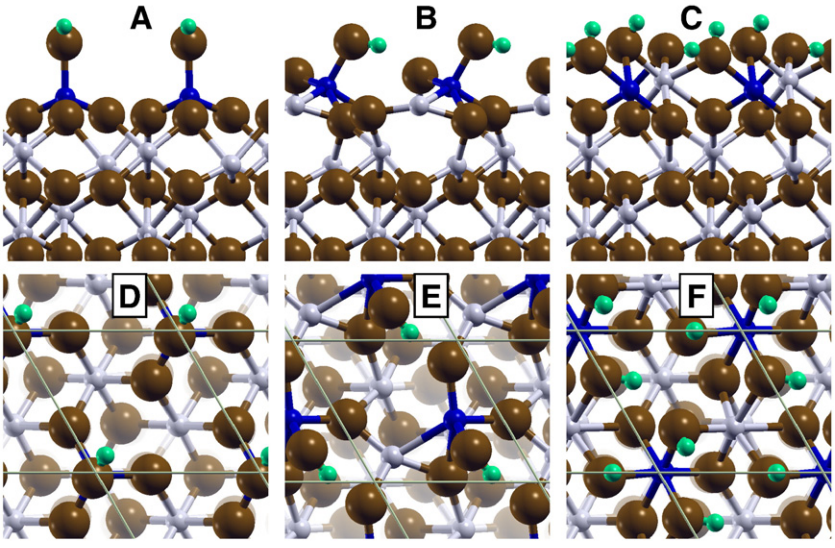

Fig. 5. Four- and six-fold coordinated 1/2 ML W hydroxylated surfaces. Top row shows side views of (A) 1/3 ML HO′ on W_A, (B) 1/3 ML HO′ on W_BFe_A, and (C) 1 ML HO′ on W_AFe_B. Bottom row shows top views of (D) 1/3 ML HO′ on W_A, (E) 1/3 ML HO′ on W_BFe_A, and (F) 1 ML HO′ on W_AFe_B. H atoms are shown in green.

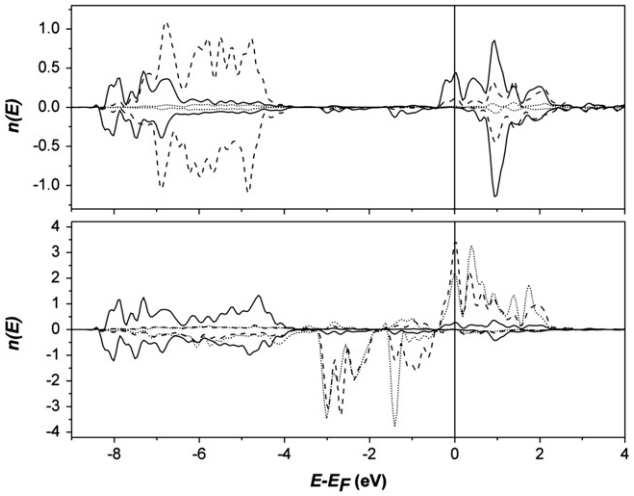

Fig. 6. Surface and near-surface atoms of HO'_AW_A (1/3 ML OH) on O-terminated hematite. Upper panel, solid W_A, dashed O'_A, and dotted H; lower panel, solid O_S, dashed Fe_C, and dotted Fe_B.

relax to bridging positions between the cations. This increases the observed coordination of W_B from 4-fold to 5-fold (Fig. 7F), although the longest W – O′ interaction, at 2.39 Å, is relatively weak. Fe_B remains 4-fold coordinated in this case.

Energetic and charge-state information about these variable coverage surface structures is compiled in Table 4B and C for O′ coverages of 0–1 ML. Data for a bulk-like Fe cation from the unrelaxed portions of the hematite slab are given for comparison in Table 4B. There is a significant energetic preference (810 meV) for the W_AFe_B configuration in the case of no overlayer O′. However, there are much smaller energetic differences between the four different 1/3 ML O′ cases examined. The $O'_BFe_BW_A$ case stands out as the *least* preferred by about 350 meV relative to the remaining three structures, which have significantly different geometries but converge to within 60 meV of each other. The $O'_BFe_BW_A$ structure (Fig. 8A) shows a strong distortion, with Fe coordinated to only two O atoms. Given the relatively small energy differences, the other three 1/3 ML O′ surface configurations could feasibly coexist under typical catalytic surface conditions. For the 2/3 ML case, a small but significant preference – 50 meV – is given to $O'_{AB}W_BFe_A$ vs. $O'_{AB}W_AFe_B$. The W_BFe_A cation configuration is preferred as well, by 350 meV, for a full O′ monolayer.

As in the case of 0.5 ML W on O-terminated surface (I) (Sec. A), there is very little variation in the spherically-integrated W net charge $Q_{WS}(W)$ with surface configuration and W – O coordination; i.e.,

$$5.37(W_AFe_B) < 5.41(O'_AW_AFe_B) \text{and} (O'_{AB}W_BFe_A) < 5.45e(O'_3W_BFe_A).$$

While the trend of increasing net charge with oxygen ligation is as expected, the magnitude of changes is small. The surface Fe orbital occupancies vary significantly more than those of W; nevertheless the net charge differences remain small. The corresponding Fe WS charge is $2.93 > 2.88 < 3.04 < 3.13$ *e*, in the same site order as above, indicating a slight oxidizing tendency with increasing O′ coordination about either metal.

Bader charges (Table 4B, C) again prove to be more sensitive to changes in the cation chemistry due to differences in the local structure. Taking again the 3-, 4-, 5-, and 6-fold W – O coordination subset of W_AFe_B, $O'_AW_AFe_B$, $O'_{AB}W_AFe_B$, and $O'_3W_BFe_A$, the W net charges $Q_B(W)$ are $1.81 < 2.41 < 2.62 < 2.86$ *e*, respectively. The corresponding Fe net charges are $0.83 > 0.81 < 1.31 < 1.69$ *e*, respectively. Interestingly, for 1/3 ML O′ coverage over W_AFe_B, both O'_A and O'_B terminations give nearly identical Fe_B charges (0.81 vs. 0.83 *e*), indicating dominance of the A-site in the local charge transfer process. Transverse dislocations in both cation sites are indicative of the rather strong local lattice distortions, reaching a maximum of 1.1 Å with no adsorbed O and diminishing to nearly perfect registry with O'_3 coverage. Further site-specific trends appear for Fe, namely that surface Fe_B atoms often have a lower charge than their isostoichiometric Fe_A counterparts. The charge on W, however, changes little with cation position, or even by the initial position of the terminal O atoms; it simply rises with increasing O coverage. The difference between chemical states for W_AFe_B vs. W_BFe_A ordering with a full O'_3 overlayer is almost indiscernible, emphasizing the subtle causes of small energy differences.

In general, W atoms on the mixed-ML cases of no or 1/3 ML O′ coverage are seen to be less oxidized compared with their W-only counterparts on O-terminated hematite (see Sec. A above), likely due to competition between the surface Fe and W species for covalency with available O. When O is plentiful, however, as in the case of 1 ML O′ coverage, the W cations on the mixed-ML surface are noticeably more oxidized than with no Fe present. The O′ layer is drawn significantly closer to the

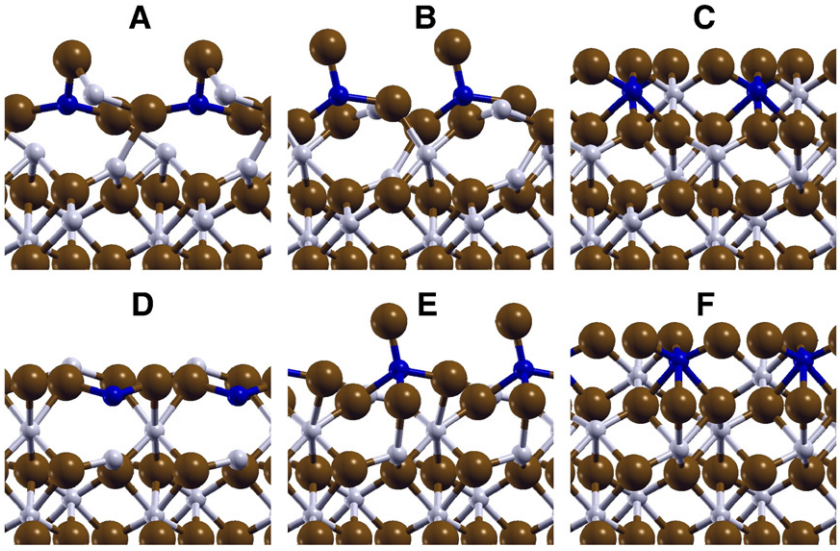

Fig. 7. Side views of three-, four-, and six-fold coordinated 1/2 ML W representing 0, 1/3, and 1 ML coadsorbed oxygen with additional surface Fe. Top row shows (A) no O′ on W_AFe_B, (B) 1/3 ML O_A' on W_AFe_B, and (C) 1 ML O′ on W_AFe_B. Structural distortions in (A) are discussed in the text. Bottom row shows (D) no O′ on W_BFe_A, (E) 1/3 ML O_B' on W_BFe_A, and (F) 1 ML O′ on W_BFe_A.

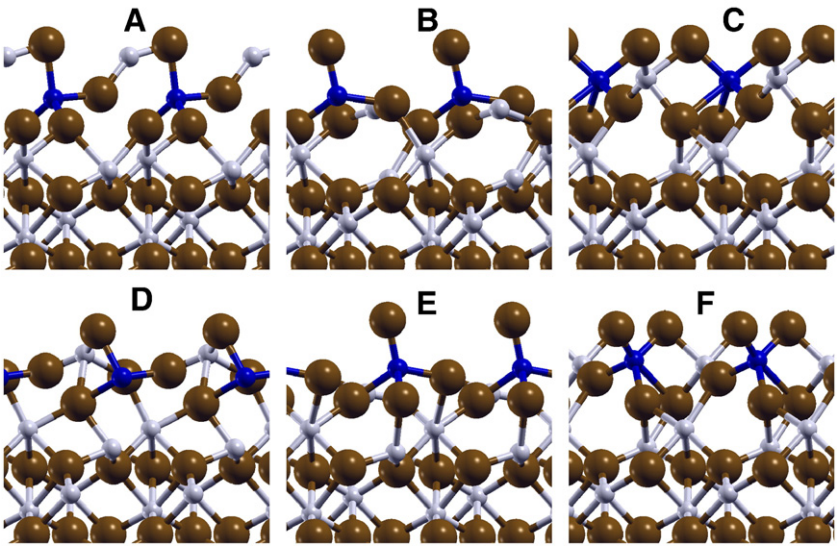

Fig. 8. Side views of four-fold coordinated 1/2 ML W representing 1/3 and 2/3 ML coadsorbed oxygen with additional surface Fe. Top row shows (A) 1/3 ML O'_B on W_AFe_B, (B) 1/3 ML O'_A on W_AFe_B, and (C) 2/3 ML O′ on W_AFe_B. Bottom row shows (D) 1/3 ML O'_A on W_BFe_A, (E) 1/3 ML O'_B on W_BFe_A, and (F) 2/3 ML O′ on W_BFe_A.

underlying surface by the presence of two cations, resulting in more substantial W – O coordination.

The partial densities of states for $O'_{AB}W_BFe_A$ and $O'_3W_BFe_A$, Fig. 9A and B, serve to illustrate differences between bimetallic coverage and single W-terminations. In contrast with the O'_AW_A structure of Fig. 3C, showing rather localized O′ and W PDOS, the adsorbed O′ 2/3 ML PDOS is seen to be broadened into a band covering essentially the entire VB region, due to its delocalization over both metal centers and interaction with the underlying O_3 substrate. The terminal Fe_A shows a well-defined spin-up band starting ~1 eV below E_F with a strong spin-down structure just above E_F, characteristic of strongly polarized bulk Fe. The W_B structure is spread over the entire VB, characteristic of its covalency with oxygen ligands, with defined excited state structures ranging over 1.5–2.5 eV above E_F. The 1 ML O'_3 spectra (Fig. 9B) show further delocalization, with displacements of both substrate and surface Fe features leading to the opening of a distinct band gap around E_F characteristic of the highly oxidized surface. The Fe magnetic structure shows some interesting features, with considerable localization indicated by narrow spin-down bands above E_F. Thus, the occupied Fe spin-up states are strongly interacting with the substrate and broadened, while non-occupied spin-down states are presumably dominant in interactions with incoming atoms and molecules.

3.3.2. Complete W coverage

Relaxed structures for a full W monolayer (W_AW_B) are provided in Fig. 10, with structural information in Tables 2B and 3B. For the case with no coadsorbed O′, W_A sits further above the O_S plane than W_B does in the z-direction. This leaves a large sub-surface hollow space as the underlying Fe_B atom is repelled downward by W_B. The W – O_S bond lengths are relatively long, at 1.91–1.98 Å. The 2/3 ML O′ overlayer model $O'_{AB}W_AW_B$, initialized with 4-fold W – O coordination for both cations, shows the expected cation z-position ordering (W_A below W_B) after relaxation. While W_B appears to be 4-fold coordinated with O, a weak fifth W – O interaction is observed at a distance of 2.69 Å. Nevertheless, the bond-average of the closest 4-coordinate shells around W_A and W_B, 1.96 and 1.99 Å respectively, suggests a slightly increased oxidation of W_A. The 1 ML O′ overlayer model $O'_3W_AW_B$ shows relatively high symmetry, exhibiting little difference in distribution of W – O distances around the 6-fold coordinated W atoms. Some distortion of the terminal O layer is observed.

For the 3-fold O-coordination state with no coadsorbed O′, the charges $Q_{WS}(W_{A,B})$ (5.29, 5.35 *e*) and $Q_B(W_{A,B})$ (1.23, 1.44 *e*) observed for the W cations (see Table 4D), are among the lowest predicted for undefected

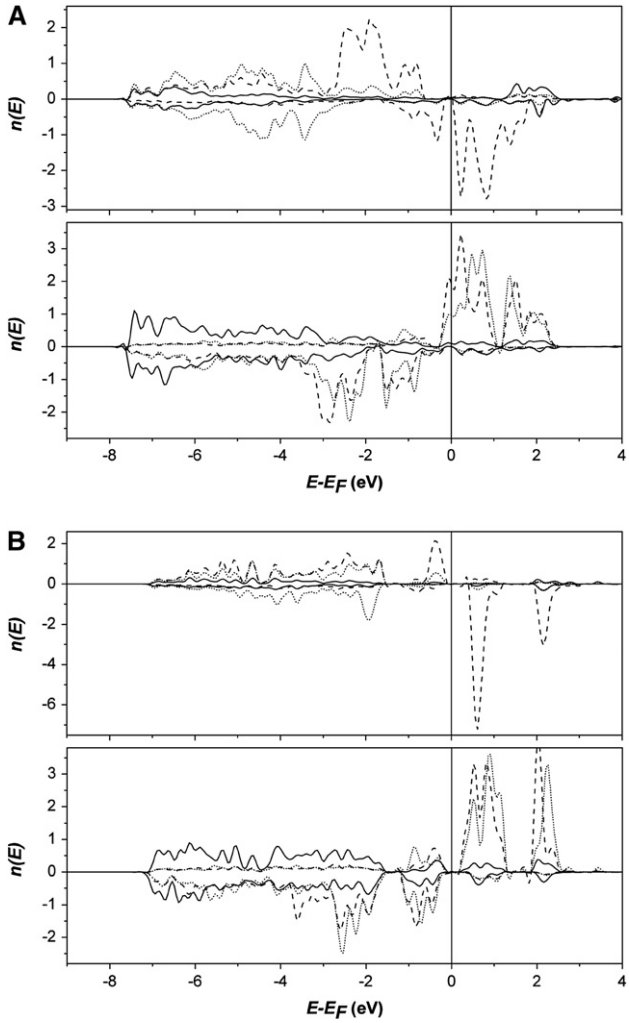

Fig. 9. (A) Surface and near-surface atoms of $O'_2W_BFe_A$ (2/3 ML O, 1 ML W) on Fe_A-terminated hematite. Upper panel, solid W_B, dashed Fe_A, and dotted O′; lower panel, solid O_S, dashed Fe_C, and dotted Fe_B. (B) Surface and near-surface atoms of $O'_3W_BFe_A$ (1 ML O′, 1/2 ML W, 1/2 ML Fe) on O-terminated hematite. Upper panel, solid W_B, dashed Fe_A, and dotted O′; lower panel, solid O_S, dashed Fe_C, and dotted Fe_B.

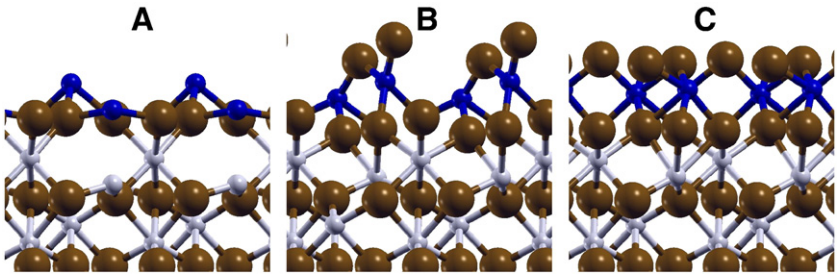

Fig. 10. Side views of three-, four-, and six-fold coordinated 1 ML W representing 1/3, 2/3, and 1 ML coadsorbed oxygen. (A) W_{AB}, (B) 2/3 ML O′ on W_{AB}, and (C) 1 ML O′ on W_{AB}.

surfaces. The predicted Bader charges for a metal-terminated W monolayer surface are lower than for a mixed W – Fe metal termination, indicating an increased competition for charge from the surface O layer. The low ionicities for the W monolayer case correspond to the long W – O_S bond lengths reported above. The 2/3 ML O′ case shows an additional increase in ionicity of 0.49–0.85 *e* from the 0 ML O′ case (as measured by the Bader method), with W_A becoming more oxidized than W_B. The corresponding Q_{WS}(W) charges increase by 0.02–0.11 *e*, again showing W_A as more oxidized, correlating to the shorter average R(W_A–O) (vs. W_B–O). With O'_3 co-adsorption, the W charges increase further: Q_B($W_{A,B}$) are 2.51, 2.53 *e* and Q_{WS}($W_{A,B}$) are 5.42, 5.42 *e* for W_A and W_B, respectively. Thus, in moving from 3- to 6-fold W – O coordination, the W Bader charges indicate a net charge transfer of 1.48 *e* in the oxidation process while the fixed-radius Q_{WS} only detects a change of 0.13 *e*. In the O'_3 case, both 6-fold coordinated W atoms are in nearly geometrically identical configurations, exhibiting little difference in ionicity and the distribution of W – O distances.

PDOS for the reduced W_AW_B surface are given in Fig. 11. The usual covalent mixing with oxygen in the VB is observed, but a strong metallic conduction band structure spanning E_F, about 4 eV in width, is also present. There is a predominance of majority spin-up character in the occupied region. Iron and oxygen substrate states are also pulled into the region around E_F, leading to the characterization of this state as highly metallic, at least in the surface region. This is explained by the additional valence electrons provided by the two W atoms; even the O band does not appear to have a gap at E_F.

3.3.3. Hydroxylated surfaces

Coadsorbed W – Fe surfaces with varying degrees of hydroxyl coverage (1/3, 2/3, 1 ML) were studied, and structural results are given in Tables 2D and 3D. The Δz vertical registry for the most stable structure for each stoichiometry is significantly altered by protonation, compared

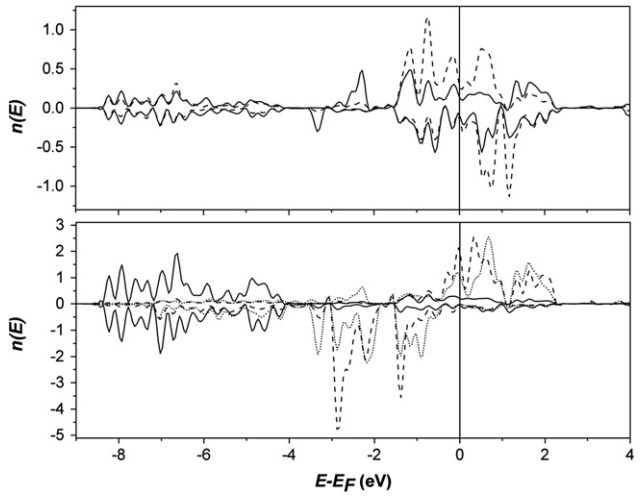

Fig. 11. Surface and near-surface atoms of 1 ML W_AW_B on O-terminated hematite. Upper panel, solid W_B and dashed W_A; lower panel, solid O_S, dashed Fe_C, and dotted Fe_B.

to O′ coverage. The interlayer spacing R_L(W – O′) increases by 0.1–0.7 Å, with the smallest change represented by $O'_BW_BFe_A \rightarrow (HO'_B)W_BFe_A$ and the largest by $O'_3W_BFe_A \rightarrow (HO')_3W_AFe_B$. For energetically favored states $O'_AW_AFe_B$ vs. $(HO'_B)W_BFe_A$, pictured in Fig. 5, the surface interlayer spacings (Table 2) shift by about 0.2 Å, while the bond lengths (Table 3) shift by 0.1–0.2 Å, with effects extending all the way down to the subsurface Fe layers. The key difference is found in R(W – O′), which extends by 0.16 Å for the hydroxylated version, while the W – O_S tetrahedron becomes more asymmetric. These relatively small bond length dilations and contractions reinforce the charge analysis conclusion (see below) that small changes in electronic structure are involved in site-switching. As just mentioned, for mono-hydroxyl coverage the $(HO'_B)W_BFe_A$ case is most favored; however, there is only a 150 meV difference between HO′ binding on W_B or Fe_A. For 2/3 and 1 ML HO′ co-adsorption, $(HO')_2W_AFe_B$ and $(HO')_3W_AFe_B$ (shown in Fig. 5) configurations are favored by 90 and 340 meV, respectively. Differing degrees of hydroxylation, attributable to reaction with hydrogen or water, can therefore modify the stable W cation site occupancy.

Charge distribution details of energetically favored hydroxylated 1 ML W – Fe structures are presented in Tables 4G and H. These can be compared directly to their O′ coadsorbed counterparts in Table 4B and C to understand the effect of hydroxylation versus oxidation. For example, comparing the most stable $O'_AW_AFe_B$ configuration with various (HO′) W – Fe possibilities, one finds that the site preference is shifted, from $(HO'_A)W_AFe_B$ to $(HO'_B)W_BFe_A$ with an energy advantage of 200 meV. Thus surface hydroxylation provides a powerful force to shift W from one site to another. Changes in cation charges upon hydroxylation, ΔQ_{WS}(W, Fe) = (+0.02, +0.09 *e*) and ΔQ_B(W, Fe) = (−0.26, −0.04 *e*) show that reconfiguration can take place with minimal perturbation of the electronic density. Q_{WS}(W) and Q_B(W) are relatively unaffected by cation position but are heavily influenced by the OH binding site. Comparing the slightly favored $(HO')_{AB}W_AFe_B$ cation ordering of the 2/3 ML hydroxyl coverage, site reversal leads to ΔQ_{WS}(W, Fe) = (+0.0, −0.03 *e*) and ΔQ_B(W, Fe) = (+0.33, −0.01 *e*) with the more reliable Bader charge indicating that W is more oxidized at the B site. Finally, for the saturated $(HO')_3$W – Fe surfaces, the W_AFe_B configuration is favored by 340 meV over its reverse, again swapping favored sites compared to $O'_3W_BFe_A$. Comparing the O'_3 vs. $(HO')_3$ charge transfers, ΔQ_{WS}(W, Fe) = (−0.01, −0.16 *e*) and ΔQ_B(W, Fe) = (−0.26, −0.35 *e*), it seems that the three OH groups capture somewhat less charge for either cation. However, the reduction implied by ΔQ_B is not as large as that caused by oxygen vacancies, as discussed next.

3.4. Effects of surface oxygen vacancies: reduction

The effects of surface oxygen vacancies causing considerable structural rearrangement on 1 ML W and Fe metal coverages are shown in Tables 2C and 3C; effective partial cation reduction is seen in Table 4E and F. The details are of some interest, since the actual experimental surfaces are doubtless defected. With the rather small supercell used here, the defect density of 1/3, 2/3 and 1 ML (complete) oxygen deficiencies may be used to track the transition from a saturated O_3 terminated surface to the Fe_B-terminated substrate. Turning now to the bimetallic W

and Fe surface models, the W_AFe_B configuration is strongly favored, by 970, 870, and 1700 meV over the W_BFe_A state for O_V, O_{V2}, and O_{V3} oxygen vacancy models, respectively. The vertical registry Δz between W_A, Fe_B, O_S, and Fe_C varies considerably (Table 2C) with vacancy concentration, ranging over 0.97–1.45 Å for W − Fe, and increasing monotonically (1.01 < 1.18 < 1.44 Å) for $Fe_{A,B,C}$. Bond lengths vary in a somewhat irregular manner (Table 3C): W_A–Fe_B ranges over 2.63 ≈ 2.55–2.88 ≈ 2.74 Å and W_A–$O_{S/S-1}$ as 1.92–2.16 ≈ 1.89–2.01 ≈ 2.03–2.09 Å. In every case the presence of surface oxygen vacancies drives a considerable structural rearrangement, with consequences for the Δz-sensitive XSW measurements. The W and Fe Bader charges follow the now familiar reduction pattern with increasing vacancy concentration: Q_B(W): 1.77 > 1.41 > 1.14 *e* and Q_B(Fe_B): 0.79 > 0.30 > 0.00 *e*. The WS volume integrated charges show a similar but weaker and less distinct trend.

4. Possible iron *d*-electron correlation effects

Due to electron localization effects and resulting correlations, LSDA and gradient expansion schemes like GGA fail to accurately predict some electronic properties, such as the bandgap, of hematite and certain other transition metal oxides [30]. In the simplified L(S)DA + U approach [31] a so-called + *U* term may be added to the Hamiltonian which introduces an additional on-site repulsive interaction between strongly correlated *d*-electrons. While the adopted total energy expression has no rigorous theoretical basis, it has the merit that its functional derivative yields the desired one-electron Hamiltonian. Furthermore, examination of the contributions of the semi-empirical correlation term has proved helpful in understanding effects of correlation in narrow band systems. Thus, the application of a + *U* correction has been shown to qualitatively modify the phase stability of hematite; for example, the high-pressure ferromagnetic phase predicted by GGA calculations is destabilized when a + *U* term is added [32]. In a similar spirit, the GGA + U method of Dudarev et al. [33] was employed here (in the so-called PW91 implementation, see Sec. II) to investigate the dependence of the electronic structure and phase stability of the WO_x/α-Fe_2O_3 (0001) surface on the value of *U*–*J*, which combines both Coulomb (*U*) and exchange (*J*) interactions. *U*–*J* values are often selected by comparison of experiment to empirical data; alternatively, an accurate *U*–*J* value of 4.3 eV for bulk α-Fe_2O_3 has recently been derived from first principles [34]. Generally speaking, the additional interaction is applied only to the partially occupied localized cation Hamiltonian matrix elements for a particular angular momentum—here, Fe *3d*. Values of *U*–*J* of 0, 2, and 4 eV for Fe *3d* states were selected to span a range of interesting values for the present investigation, and simply referred to as *U* in the following. No such terms were contemplated for the W atoms.

The relative stabilities of different surface structures determined at different *U* values are shown in Table 5. Cases shown include 1/3 ML O′ atop 1/2 ML W and mixed-metal surfaces as well as 2/3 ML O′ atop mixed-metal surfaces. The structures were relaxed at *U* = 0 eV, and their electronic states were re-converged at *U* = 2 and 4 eV. For the 2/3 ML O′ case, the addition of a *U* value changed the energy difference between the isostoichiometric structures, increasing the stability of the $O'_{AB}W_BFe_A$ configuration by 140–200 meV versus the $O'_{AB}W_AFe_B$ case. The relative stability of the O'_AW_A case compared to the O'_BW_B dropped insubstantially at *U* = 2 eV. For the 1/3 ML O′ on 1/2 ML W cases, no acceptable electronic convergence could be achieved for *U* = 4 eV.

The addition of a *U* term yielded more interesting results, however, for the 1/3 ML O′ on mixed-metal terminated surfaces. Without a *U* term, the $O'_AW_AFe_B$ configuration is slightly more stable than the two W_BFe_A structures, with O′ sitting over either the W or Fe. However, the addition of a *U* = 2 eV term significantly destabilizes the W_AFe_B configuration, instead favoring the opposite arrangement by 120–150 meV, with the O′ bound to the Fe_A atom (which actually relaxes to a more bridging configuration between W and Fe, see Fig. 3) in the most stable condition. Increasing the *U* value to 4 eV shifts the stable coordination of the O′ atom from a bridging position between cations to the W_B atom exclusively. Since the + *U* procedure amounts to opening a gap between occupied and vacant Fe *d* states, we can infer that resulting shifts in *s*–*d* and *p*–*d* hybridization and accompanying Fe–O covalency are sufficient to modify relative stability of surface structures. The variability of W *4d* occupancy upon hydroxylation, discussed above, suggests that future GGA + U studies should focus equally upon Fe and W correlation effects; however, exploring such two-parameter models will be nontrivial.

5. Core level spectra and comparison with XSW, XAFS and XPS experiments

Previously, plausible surface structures were proposed for the nominally "reduced" (via exposure to H_2) and "oxidized" surfaces (referred to as *Re* and *Ox*, respectively) for 1/3 ML W on hematite (0001) [8]. XSW results provided the proposed W ion position, while X-ray absorption fine structure (XAFS) suggested a saturated oxygen coordination of 6 for the *Ox* case. Models resulting from fits to XSW amplitude and phase data suggest that the position of the coherent fraction of W on hematite (0001) remains well-centered above Fe surface sites, moving in the (0001) surface normal direction upon undergoing chemical change [6,8]. Thus, in order to correlate theoretical predictions given above with XSW data, the W z-position must be compared to the bulk-like Fe positions. The fact that roughly 35–55% of surface-adsorbed W is not 'visible' (based upon Atomic Layer Deposition (ALD) dosage [35,36] and subsequent X-ray fluorescence intensities compared with the XSW coherent fraction), and thus not in registry with the underlying cation lattice, leads one to suppose that there exist further energetically attractive surface sites, perhaps associated with native defects. With the small supercells used in the present work, we are unable to offer concrete structural models for this missing fraction (however, note comments above on transverse cation displacements in defected structures), and instead search for the closest match to experiment between calculated Δz values and energetically favored sites in a given redox environment.

As to comparisons with XPS experimental data, we have seen via the Bader charge analysis that the general expectations of oxidation state vs. oxygen coordination are fulfilled, with local cation charge variations ΔQ_B being less, by almost 50%, than that expected from nominal high-valence configurations. This is certainly not a surprise in light of a wealth of theoretical studies on ionic-covalent compounds, and helps to motivate more subtle considerations based upon energetics.

Given the considerable number of surface configurations and non-stoiochiometric compositions studied, it is not surprising that certain 'reduced' and 'oxidized' models adequately reproduce the XSW results for lattice site and position. Fortunately, those models are found to be of low energy and relatively stable compared to other cases, lending some credence to the identification (Table 6). It is particularly interesting to consider the predicted ground state configuration of W_BFe_A in the

Table 5
Comparison of converged energies of PW91 + *U* model for selected relaxed configurations. The numbers shown are E–E_S, where E is the converged total supercell cohesive energy in eV and E_S is the converged total supercell energy for the most stable isostoichiometric supercell.

U (eV)	O'_AW_A	O'_BW_B	$O'_AW_AFe_B$	$O'_AW_BFe_A$	$O'_BW_BFe_A$	$O'_{AB}W_AFe_B$	$O'_{AB}W_BFe_A$
0	0.00	−0.84	0.00	−0.06	−0.02	−0.05	0.00
2	0.00	−0.80	−0.16	0.00	−0.03	−0.25	0.00
4	–	–	−0.13	−0.05	0.00	−0.19	0.00

oxidized state as well as the likely protonation at a fraction of reduced W sites. Additionally, the poor match of 1 ML W_AW_B calculations to XSW results suggests that the deposited 1/3 ML WO_x films did not grow as atomically thin, W-dense rafts or islands. The better match with the 1/2 ML cases implies that the WO_x was more evenly dispersed over the sample surface. However, the small unit cell size precludes any strong conclusions regarding such long-range effects.

Tungsten $4f_{5/2,\ 7/2}$ XPS core-level measurements on surfaces and non-stoichiometric films and particles typically give values of W^{6+} (35.6, 37.7 eV) and W^{5+} (34.5, 36.6 eV) [37,38], revealing a spin–orbit splitting of 2.1 eV and a oxidation-state shift of 1.1 eV. A number of molecular cluster calculations were carried out in the Transition State scheme described previously, in an effort to identify theoretical core-level shifts with changes in W chemical environment. Since the core-hole effects are essentially Coulombic in nature, with energy differences due mostly to electronic screening from the environment, we may examine the difference of two environments using *non-relativistic* models. Later, one may use the fully relativistic Dirac-Slater scheme to resolve the spin–orbit splitting of the core states and for further detailed studies of such multielectron phenomena as shake-up, shake-down, and Auger transitions. Calculated core-level energies taken relative to the local Fermi energy show a variation of 1.19 eV over the various W coordination environments, in quantitative agreement with experiment. However, we are not able to cleanly identify only two distinct valence states; indeed, we find a range of values between the extreme limits. This may not be too surprising, as the models contain 3-, 4-, 5-, and 6-fold coordinated W, some of which may not be stable on the experimental surfaces. It would be interesting to carry out more systematic studies with larger embedded clusters and inclusion of spin–orbit effects to obtain a more quantitative picture.

6. Conclusions

Using DFT, various reduced and oxidized configurations of tungsten on the hematite (0001) surface have been explored, using both ground state band structure and localized-orbital W core-hole models. Adsorption of W on surfaces with compositions ranging from oxygen saturated to Fe terminated was considered, as were coadsorption with iron, oxygen, or hydroxyl groups. By comparing calculated relaxed structural and electronic data to experiment, one obtains a good match with site-specific XSW data for nominally oxidized and reduced configurations. Low energy configurations give a best fit to experiment, lending confidence to the theoretical approach. Experimental W *4f* XPS data which show reversible oxidation and reduction of W on the surface are quantitatively reproduced by Transition State cluster calculations. However, it was not possible to identify distinct "W^{5+}" and "W^{6+}" oxidation states in cluster models containing 3-, 4-, 5-, and 6-fold coordinated tungsten; rather, a continuous variation of net charge and core-level energies was observed. As found in many other theoretical studies, cation charges are calculated to be notably less than nominal oxidation-state values (Fe^{3+}, W^{5+}, W^{6+}), whether defined by spherically-integrated R_{WS} charges or by the zero-flux surface Bader approach. The characteristic trends of increasing cation charge with oxygen coordination and the associated metal–oxygen bond length variations are reported. The possible effects of Fe *3d* correlation corrections on surface structures were considered, using the GGA + U approach. It was found that some re-ordering of site energies could occur; however, the lack of knowledge of optimized surface-related values of the parameter *U* (applied only to Fe and not W) renders doubtful any strong predictions.

The small crystal unit cells and small molecular clusters used in this work preclude any study of larger scale phenomena such as surface reconstruction, metal agglomeration, coexistence of different W oxidation states, and raft/cluster formation. The use of such small surface cells may also result in a "periodic image" effect caused by the lateral interaction between an atom and itself in a neighboring identical cell. The present work therefore serves as an adequate launch point for more extensive modeling, including larger surface unit cells and interactions with adsorbing molecules.

Table 6
Comparison of W A- and B-site z displacements above the bulk-like O_3 plane derived from XSW experiment with selected energetically favored DFT-calculated configurations.

	Experiment[a] "reduced"	O'_AW_A	HO'_AW_A	$O'_{AB}W_BFe_A$	Experiment[a] "oxidized"	$O'_3W_BFe_A$
z_A	0.88	0.79	0.89	–	–	–
z_B	1.46	–	–	1.51	1.54–1.58	1.58

[a] Ref. [8].

Acknowledgments

This research was supported in part by the Chemical Sciences, Geosciences and Biosciences Division, Office of Basic Energy Sciences, Office of Science, US Department of Energy, Grant No. DE-FG02-03ER15457, at the Institute for Catalysis in Energy Processes at Northwestern University. Additional support was received from the Initiative for Sustainability and Energy at Northwestern University. This material is partially based upon work supported by the National Science Foundation Graduate Research Fellowship under Grant No. DGE-0824162. Use of the APS at Argonne National Laboratory was supported by the DOE-BES under Contract No. W-31-109-ENG-38. DND-CAT is supported in part by the State of Illinois.

Appendix A. Supplementary data

Supplementary data to this article can be found online at http://dx.doi.org/10.1016/j.susc.2012.04.023.

References

[1] V.E. Henrich, P.A. Cox, The Surface Science of Metal Oxides, Cambridge University Press, 1994.
[2] B. Weckhuysen, D. Keller, Catal. Today 78 (2003) 25.
[3] W. Weiss, W. Ranke, Prog. Surf. Sci. 70 (2002) 1.
[4] J. Jin, X. Ma, C.-Y. Kim, D.E. Ellis, M.J. Bedzyk, Surf. Sci. 601 (2007) 3082.
[5] J. Jin, X. Ma, C.-Y. Kim, D.E. Ellis, M.J. Bedzyk, Surf. Sci. 601 (2007) 4571.
[6] C.-Y. Kim, A.A. Escuadro, P.C. Stair, M.J. Bedzyk, J. Phys. Chem. C 111 (2007) 1874.
[7] S.L. Soled, G.B. McVicker, L.L. Murrell, L.G. Sherman, N.C. Dispenziere Jr., S.L. Hsu, D. Waldman, J. Catal. 111 (1988) 286.
[8] Z. Feng, C.-Y. Kim, J.W. Elam, Q. Ma, Z. Zhang, M.J. Bedzyk, J. Am. Chem. Soc. 131 (2009) 18200.
[9] L. Lietti, J.L. Alemany, P. Forzatti, G. Busca, G. Ramis, E. Giamello, F. Bregani, Catal. Today 29 (1996) 143.
[10] L. Ferretto, A. Glisenti, J. Mol. Catal. A 187 (2002) 119.
[11] P.E. Boahene, K.K. Soni, A.K. Dalai, J. Adjaye, Appl. Catal. A 402 (2011) 31.
[12] G. Kresse, J. Furthmüller, Phys. Rev. B 54 (1996) 11169.
[13] G. Kresse, J. Furthmüller, Comput. Mater. Sci. 6 (1996) 15.
[14] G. Kresse, J. Hafner, Phys. Rev. B 47 (1993) 558.
[15] G. Kresse, J. Hafner, Phys. Rev. B 49 (1994) 14251.
[16] P.E. Bloechl, Phys. Rev. B 50 (1994) 17953.
[17] J.P. Perdew, J.A. Chevary, S.H. Vosko, K.A. Jackson, M.R. Pederson, D.J. Singh, C. Fiolhais, Phys. Rev. B 46 (1992) 6671.
[18] I.de.P.R. Moreira, F. Illas, R.L. Martin, Phys. Rev. B 65 (2002) 155102.
[19] N.C. Wilson, S.P. Russo, Phys. Rev. B79 (2009) 094113.
[20] H.J. Monkhorst, J.D. Pack, Phys. Rev. B 13 (1976) 5188.
[21] P. Pulay, Chem. Phys. Lett. 73 (1980) 393.
[22] G. Henkelman, A. Arnaldsson, H. Jónsson, Comput. Mater. Sci. 36 (2006) 354.
[23] Local perturbations are not well treated in periodic cells due to interaction between adjacent cells. In principle this can be overcome by using sufficiently large supercells. In the present case, long range Coulomb–hole interactions would require prohibitively large cells.
[24] D.E. Ellis, D. Guenzburger, Adv. Quantum Chem. 34 (1999) 51 (and references therein).
[25] A.R. Williams, R.A. deGroot, C.B. Sommers, J. Chem. Phys. 63 (1975) 628.
[26] W. Bergermayer, H. Schweiger, E. Wimmer, Phys. Rev. B 69 (2004) 195409.
[27] X.-G. Wang, W. Weiss, Sh.K. Shaikhutdinov, M. Ritter, M. Petersen, F. Wagner, R. Schlögl, M. Scheffler, Phys. Rev. Lett. 81 (1998) 1038.
[28] S. Polarz, J. Strunk, V. Ischenko, M. van den Berg, O. Hinrichsen, M. Muhler, M. Driess, Angew. Chem. Int. Ed. 45 (2006) 2965.
[29] M. Aizawa, Y. Morikawa, Y. Namai, H. Morikawa, Y. Iwasawa, J. Phys. Chem. B 109 (2005) 18831.
[30] A. Svane, O. Gunnarsson, Phys. Rev. Lett. 65 (1990) 1148.
[31] V.I. Anisimov, J. Zaanen, O.K. Andersen, Phys. Rev. B 44 (1991) 943.

[32] G. Rollmann, A. Rohrbach, P. Entel, J. Hafner, Phys. Rev. B 69 (2004) 165107.
[33] S.L. Dudarev, G.A. Botton, S.Y. Savrasov, C.J. Humphreys, A.P. Sutton, Phys. Rev. B 57 (1998) 1505.
[34] N.J. Mosey, P. Liao, E.A. Carter, J. Chem. Phys. 129 (2008) 014103.
[35] J.W. Elam, C.E. Nelson, R.K. Grubbs, S.M. George, Thin Solid Films 386 (2001) 41.
[36] Z.A. Sechrist, F.H. Fabreguette, O. Heintz, T.M. Phung, D.C. Johnson, S.M. George, Chem. Mater. 17 (2005) 3475.
[37] M. Sun, N. Xu, Y.W. Cao, J.N. Yao, J. Mater. Res. 15 (2000) 927.
[38] K. Senthil, K. Yong, Nanotechnology 18 (2007) 395604.